Chemical Science

ROYAL SOCIETY OF CHEMISTRY

EDGE ARTICLE

View Article Online
View Journal | View Issue

Cite this: *Chem. Sci.*, 2023, **14**, 5415

All publication charges for this article have been paid for by the Royal Society of Chemistry

Received 5th April 2023
Accepted 22nd April 2023

DOI: 10.1039/d3sc01762a

rsc.li/chemical-science

Photophysical studies for Cu(I)-based halides: broad excitation bands and highly efficient single-component warm white-light-emitting diodes†

Shuigen Zhou, Yihao Chen, Kailei Li, Xiaowei Liu, Ting Zhang, Wei Shen, Ming Li, Lei Zhou * and Rongxing He *

Designing and synthesizing cuprous halide phosphors unifying efficient low-energy emission and a broad excitation band is still a great challenge. Herein, by rational component design, three novel Cu(I)-based metal halides, $DPCu_4X_6$ [DP = $(C_6H_{10}N_2)_4(H_2PO_2)_6$; X = Cl, Br, I], were synthesized by reacting *p*-phenylenediamine with cuprous halide (CuX), and they show similar structures, consisting of isolated $[Cu_4X_6]^{2-}$ units separated by organic layers. Photophysical studies uncover that the highly localized excitons and rigid environment give rise to highly efficient yellow-orange photoluminescence in all compounds with the excitation band spanning from 240 to 450 nm. The bright PL in $DPCu_4X_6$ (X = Cl, Br) originates from self-trapped excitons due to the strong electron–phonon coupling. Intriguingly, $DPCu_4I_6$ features a dual-band emissive characteristic, attributed to the synergistic effect of halide/metal-to-ligand charge-transfer (X/MLCT) and triplet cluster-centered (^{3}CC) excited states. Benefiting from the broadband excitation, a high-performance white-light emitting diode (WLED) with a high color rendering index of 85.1 was achieved using single-component $DPCu_4I_6$ phosphor. This work not only unveils the role of halogens in the photophysical processes of cuprous halides, but also provides new design principles for high-performance single-component WLEDs.

Introduction

Organic–inorganic hybrid metal halides have attracted great interest because of their special electronic structures and optical properties.[1–4] Different combinations of organic cations and metal–halide clusters enable rich structures with various physical and optical properties.[5–10] In addition, hybrid metal halides have many advantages such as high defect tolerance, adjustable energy bands and convenient synthesis methods, making them a great commercial prospect in solid-state lighting (SSL), scintillators, anti-counterfeit encryption, *etc.*[1,11–15] Due to the unique $6s^2$ lone-pair electronic configuration of Pb^{2+}, lead-based metal halides tend to show excellent optoelectronic performance.[16] In fact, a large number of lead-halide perovskites with outstanding luminescence properties have been developed in recent years.[17–19] However, the inherent toxicity of lead is a great threat to the environment and people's health, and thus lead-free metal halides have attracted enormous interest.[20]

Among the alternatives, cuprous-based halides have developed rapidly due to their low price, low toxicity and outstanding optical performance, and are one of the promising candidates for the new generation of light-emitting materials.[21–23] Although multiple cuprous-based materials with admirable photoluminescence quantum yield (PLQY) including $(Gua)_3Cu_2I_5$,[24] $[N(C_2H_5)_4]_2Cu_2Br_4$,[25] $(MA)_4Cu_2Br_6$,[26] and $(AEP)_2Cu_2I_6\cdot 2I\cdot 2H_2O$[27] have been reported, their further development faces at least the following two problems to be solved: (1) most reported Cu(I)-based halides with high PLQY are blue-green and white emitters; (2) they typically require deep ultraviolet (UV) excitation, in other words, their PL excitation (PLE) spectrum is not broad enough to meet the excitation requirement. Therefore, it is of great significance to develop low-energy light emitting cuprous-based materials with a broad excitation band.

Compared with all-inorganic metal halides, organic–inorganic hybrid metal halides are more flexible and convenient in selecting cations to be paired with metal–halogen clusters, thus inspiring researchers to design and synthesize crystalline materials with different structural dimensionality and photophysical properties. In fact, some principles for selecting appropriate organic cations have been proposed to achieve

Key Laboratory of Luminescence Analysis and Molecular Sensing (Southwest University), Ministry of Education, School of Chemistry and Chemical Engineering, Southwest University, Chongqing 400715, China. E-mail: zhoulei25@swu.edu.cn; herx@swu.edu.cn

† Electronic supplementary information (ESI) available: Experimental materials and methods for sample preparation; computational methods; detailed crystallographic results; supplementary figures including digital photos of the samples, CIE, PLE, PL, PLQY, TRPL, XPS. CCDC 2236271, 2236273 and 2253788. For ESI and crystallographic data in CIF or other electronic format see DOI: https://doi.org/10.1039/d3sc01762a

excellent optoelectronic properties. For example, large distorted polyhedral clusters and low-dimensional structures are conducive to the formation of self-trapped excitons (STEs), while emissions from STEs accompanied by large Stokes shifts tend to generate low-energy emission bands, so that large-sized organic cations are preferred in order to achieve yellow-red light emission.[28–34] Further, moderate structural rigidity is beneficial to reduce lattice vibration and inhibit nonradiative recombination, which is confirmed in many compounds such as $(EnrofloH_2)SnCl_6 \cdot H_2O$,[6] $(C_9H_8N)_2SnCl_6$,[35] *etc.* Therefore, to enable materials with low-energy emission as well as high PL efficiency, aromatic polyamine compounds with rigid structures are often considered as organic cations to support the low dimensionality. In addition, the emission band can be efficiently tuned by changing the halogen anions.[36] For lighting application, broadband excitation as well as emission from a single emitter are highly expected, because it can simplify the device structure and avoids the self-absorption and color instability often observed in mixed and multiple emitters.

Herein, the rigid bis-ammonium aromatic compound *p*-phenylenediamine was adopted to synthesize a range of novel cuprous-based halides $DPCu_4X_6$ [$DP = (C_6H_{10}N_2)_4(H_2PO_2)_6$; X = Cl, Br, I] by reacting with CuX. As a result, three compounds crystallized in zero-dimensional (0D) structures composed of hydrogen-bonded organic layers and spatially isolated $[Cu_4X_6]^{2-}$ clusters. The resultant materials achieve a wide PLE spectrum and highly efficient orange/yellow light emission, making these materials attractive for practical application. Comprehensive experimental and theoretical investigations show that the bright luminescence of the chloride and bromide originates from STEs, while the efficient emission of the iodide is attributed to the synergistic effect of halide/metal-to-ligand charge-transfer (X/MLCT) and cluster-centered (^{3}CC) excited states. In addition, considering the excellent optical properties (broad excitation and emission bands) and the remarkable stability of $DPCu_4I_6$, a white-light emitting diode (WLED) with a high CRI was successfully manufactured using single-component $DPCu_4I_6$ powder excited with a 445 nm blue light chip, demonstrating the practical application potential of these new materials.

Results and discussion

$DPCu_4X_6$ (X = Cl, Br, I) single crystals (SCs) were prepared using a facile cooling crystallization method. Briefly, *p*-phenylenediamine and cuprous halide CuX (X = Cl, Br, I) were dissolved in a mixture of acetonitrile and hypophosphorous acid (H_3PO_2) solution at 120 °C to form a colorless transparent solution. By slowly decreasing the temperature of the mixture to room temperature (RT), target compounds were obtained (see details in the ESI†). Although the CuX precursors used for the synthesis of the three compounds are different, the resultant products ($DPCu_4Cl_6$, $DPCu_4Br_6$, and $DPCu_4I_6$) show similar morphologies, being square and transparent shapes with a side length of about 5 mm (Fig. S1†). Under natural light, $DPCu_4Cl_6$ and $DPCu_4Br_6$ SCs are colorless, while $DPCu_4I_6$ SCs are yellow. Under 365 nm ultraviolet (UV) lamp irradiation, $DPCu_4Br_6$ and $DPCu_4I_6$ SCs emit bright yellow light, while $DPCu_4Cl_6$ SCs emit orange light. The structures of the three compounds were analyzed by a single-crystal X-ray diffraction (SCXRD) technique. $DPCu_4Cl_6$ crystallizes in the orthorhombic structure system with the space group of *Ccca*, and $DPCu_4Br_6$ and $DPCu_4I_6$ belong to the tetragonal system with space groups $I4_1/acd$ and $P4/m$, respectively. Because of the almost similar synthetic methods and conditions for them, the structures of $DPCu_4X_6$ have some identical features. As shown in Fig. 1a and S2,† through the alternate stacking of organic and inorganic layers, all these crystals form a sandwich structure. The organic layers are composed of *p*-phenylenediamine cations ($[C_6H_{10}N_2]^{2+}$) and hypophosphite anions ($[H_2PO_2]^-$), in which the oxygen atoms on the $[H_2PO_2]^-$ are closely linked to the $(C_6H_{10}N_2)^{2+}$ through hydrogen bonds whose length is less than 3 Å (Fig. 1c and Table S2†). It is worth mentioning that since we did not use hydrohalic acid as a solvent during the synthesis, the amount of halogen ions in the solution was not sufficient to balance the positive charge, so the added $[H_2PO_2]^-$ anions not only play a role in the Cu^{2+} reduction, but also participate in the structural construction. The introduction of $[H_2PO_2]^-$ anions may bring some beneficial effects for efficient luminescence. First, it can form abundant hydrogen bonds between the components of the crystal, thereby enhancing the rigidity of the crystal structure;[37] second, it can lengthen the distance between clusters, leading to stronger exciton localization. Although these crystals resemble planar two-dimensional structures, metal–halide polyhedrons in the inorganic layers are indeed isolated, and the $[Cu_4X_6]^{2-}$ clusters are periodically embedded in the organic matrix to form a unique 0D structure (Fig. 1b). In such structures, each Cu^+ is coordinated with three X^- to form a plane triangular configuration of CuX_3, and then four congruent CuX_3 units are interconnected and shared through triangular edge nodes to form a hollow Cu-halogen octahedral cluster (Fig. 1c, S2c, and S2f†). Similarly, it can also be understood that six halogen atoms form a slightly distorted octahedron, and four copper atoms are embedded in the four faces of the octahedron. The four Cu atoms of each $[Cu_4X_6]^{2-}$ (X = Cl or Br) cluster in $DPCu_4Cl_6$ and $DPCu_4Br_6$ form a Cu_4 tetrahedron, while

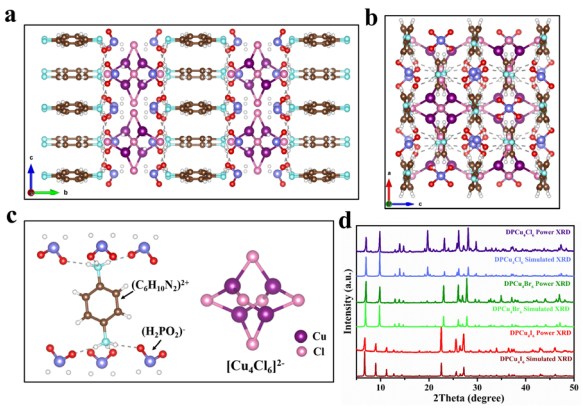

Fig. 1 Crystal structure of $DPCu_4Cl_6$ viewed along the (a) *a* axis and (b) *b* axis (Cu, purple; Cl, pink; P, blue; O, red; C, brown; N, cyan; H, white). (c) Individual $[Cu_4Cl_6]^{2-}$ cluster and $[C_6H_{10}N_2]^{2+}$ organic cation. Note that each $[C_6H_{10}N_2]^{2+}$ links with six $[H_2PO_2]^-$ anions through hydrogen bonds. (d) PXRD and SCXRD patterns of $DPCu_4X_6$ (X = Cl, Br, I) SCs.

the Cu site in a $[Cu_4I_6]^{2-}$ anion has 50% occupancy, *i.e.*, the two groups of non-edge-sharing octahedron faces form two Cu_4 tetrahedra, one of which is inverted with respect to the other, resulting in the half-weighted Cu. The Cu–Cu bond distance in $DPCu_4I_6$ is 2.51–2.96 Å, which shows that the Cu–Cu metal bond exists in the iodide and suggests strong Cu–Cu bonding interactions in this cluster.[38] The average Cu–Cu bond distances for $DPCu_4Cl_6$ and $DPCu_4Br_6$ are 2.82 Å and 2.89 Å, respectively, indicating that the Cu–Cu interaction in these two compounds is weaker than the iodide. Furthermore, the distance between two adjacent $[Cu_4X_6]^{2-}$ clusters is over 6 Å, excluding electronic interactions between them. The powder X-ray diffraction (PXRD) patterns of $DPCu_4X_6$ agree well with those from SCXRD, suggesting the high purity and uniformity of the as-synthesized crystals (Fig. 1d). In addition, the hydrogen nuclear magnetic resonance (^{1}H-NMR) spectra of $C_6H_{10}N_2Cl_2$ and $DPCu_4Cl_6$ shown in Fig. S3 and S4† show that the peaks in the spectra are almost identical without peaks of impurity appearing, further confirming the high purity of the synthesized compounds. X-ray photoelectron spectroscopy (XPS) measurements in Fig. S5† confirm that $DPCu_4X_6$ (X = Cl, Br, I) contains the elements of C, H, N, O, P, Cu and X, which agrees with the SCXRD analysis. The high-resolution Cu 2p spectra of $DPCu_4X_6$ show two peaks at 931.8 eV and 951.8 eV, verifying the +1 oxidation state of Cu.[39]

In order to explore the optical properties of $DPCu_4X_6$ SCs, steady-state PL/PLE spectra of the as-synthesized SCs were characterized at RT (Fig. 2a). Surprisingly, all three compounds exhibit broad-band PLE spectra covering 240–450 nm, which is beneficial for the SSL applications. It can be clearly observed that the PLE spectra of $DPCu_4Cl_6$ and $DPCu_4Br_6$ have similar shapes and characters, while that of $DPCu_4I_6$ displays an opposite shape with a wider bandwidth. The $DPCu_4Cl_6$ SCs exhibit a single broad-band emission peaked at 612 nm with a full width at half-maximum (FWHM) of 148 nm and a large Stokes shift of 245 nm. While both the $DPCu_4Br_6$ and $DPCu_4I_6$ SCs emit bright yellow light with the same emission peak at 575 nm. The Stokes shift of $DPCu_4Cl_6$ and $DPCu_4I_6$ is 198 and 282 nm, respectively. The FWHM of $DPCu_4I_6$ is 185 nm, which is broader than that of $DPCu_4Br_6$ (123 nm). Accordingly, the Commission Internationale de L'Eclairage (CIE) chromaticity coordinate is calculated to be (0.52, 0.45) for $DPCu_4Cl_6$, (0.45, 0.51) for $DPCu_4Br_6$ and (0.43, 0.49) for $DPCu_4I_6$, respectively (Fig. 2b). When the temperature is decreased to 80 K, the PL and PLE spectra of the three halides become narrower (Fig. 2c). Both $DPCu_4Cl_6$ and $DPCu_4Br_6$ maintain a Gaussian-shaped single peak. The maximum peak position of the bromide remains unchanged, while that of the chloride red shifts to 650 nm. The shape and characteristics of the PLE spectra of $DPCu_4Cl_6$ and $DPCu_4Br_6$ have hardly changed. However, the spectral characteristics of $DPCu_4I_6$ SCs have changed at 80 K. Herein, its PLE spectrum splits to multiple peaks and its emission spectrum contains dual-band emissions with a high-energy (HE) one peaked at 600 nm and a low-energy (LE) peaked at 703 nm. The transient PL (TRPL) decay dynamics was also measured at RT to probe the optical properties of the compounds. As revealed in Fig. 2d, both $DPCu_4Cl_6$ and $DPCu_4Br_6$ have a long lifetime more than 40 μs monitored at 600 nm, similar to some low-dimensional Cu(I)-based metal halides, such as CuCl-am[40] and $(18\text{-crown-}6)_2Na_2(H_2O)_3Cu_4Br_6$.[41] The PL decay time of $DPCu_4I_6$ is significantly faster, with a lifetime of 4.30 μs monitored at 600 nm and 4.62 μs monitored at 700 nm (Fig. S6†). It is worth noting that

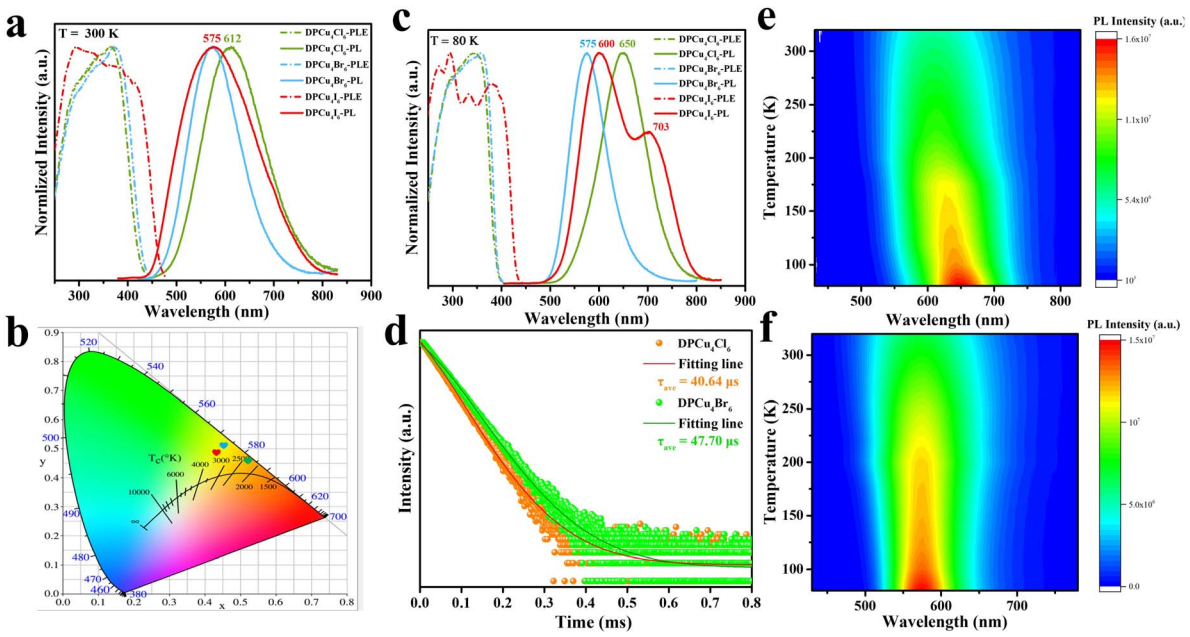

Fig. 2 PL and PLE spectra of $DPCu_4X_6$ (X = Cl, Br, I) SCs measured at (a) 300 K and (c) 80 K (excited at 320 nm, monitored at 600 nm). (b) CIE chromaticity diagram of $DPCu_4X_6$ ($DPCu_4Cl_6$, green; $DPCu_4Br_6$, red; $DPCu_4I_6$, blue). (d) The RT-TRPL spectra of $DPCu_4X_6$ (X = Cl, Br) SCs probed at 600 nm. Temperature-dependent PL spectra of (e) $DPCu_4Cl_6$ and (f) $DPCu_4Br_6$.

the PLQY of the three halides is very high, 89.76% for $DPCu_4Cl_6$, 93.52% for $DPCu_4I_6$, and even 95.04% for $DPCu_4Br_6$ SCs (Fig. S7 and Table S3†). Most reported Cu(I)-based metal halides usually exhibit blue or green emission. Even if there are a few reported materials emitting yellow/orange light, their excitation bands are either narrow or located in the high-energy UV region (<350 nm), which hinders the further lighting applications (Table S3†). Therefore, low-energy emissive (yellow to red light) Cu(I)-based materials with a broad PLE spectrum are highly attractive. Fortunately, $DPCu_4X_6$ SCs can meet the above requirements well.

Spectroscopic characterization at RT and 80 K indicates that $DPCu_4Cl_6$ and $DPCu_4Br_6$ have similar PL emission characteristics, while a complex luminescence mechanism may be hidden within the $DPCu_4I_6$ SCs. To further explore the changes of the radiative mechanism caused by the halogen substitution, the potential photophysical mechanism of $DPCu_4Cl_6$ and $DPCu_4Br_6$ was first studied. As shown in Fig. S8,† wavelength-dependent PL/PLE spectra of $DPCu_4X_6$ (X = Cl or Br) were recorded at RT, where the identical features of the spectrum suggest that the broadband emission of the halide should stem from the same excited state. The PL spectra of $DPCu_4X_6$ (X = Cl or Br) measured at 80 K with different excitation wavelengths have the same profile, further confirming such an inference (Fig. S9†). The PL intensity of the chloride and bromide increases monotonically and linearly with the increase of excitation power, which excludes the effect of permanent defects on the emission (Fig. S10†). In a word, the typical optical features with a large Stokes shift, broad emission band, high PLQY and long PL lifetime strongly support that the bright orange/yellow emission from $DPCu_4Cl_6$ and $DPCu_4Br_6$ is related to the STEs.[2,42–45] The strong coupling between the exciton and lattice could lead to the elastic lattice to deform transiently, and then form photoinduced trap states below the conduction band. Once the photogenerated excitons are produced, they will be rapidly self-trapped by the STE energy level, and then the excitons return to the ground state through emitting photons with a large Stokes shift and microsecond lifetime.[3]

Subsequently, the temperature-dependent PL measurement of $DPCu_4Cl_6$ and $DPCu_4Br_6$ was carried out at 80–300 K to further understand the emission mechanism (Fig. 2e and f). It is found that the PL spectra of the two materials have only one emission peak in the whole temperature range, indicating the single radiative mechanism. Note that the maximum emission wavelength of $DPCu_4Cl_6$ gradually increases with the decrease of test temperature, while that of $DPCu_4Br_6$ is almost independent of temperature. In fact, this phenomenon that the emission peak position of chloride is more temperature-dependent than that of bromide has been observed in many all-inorganic and organic–inorganic hybrid Cu(I)-based materials.[40,46] The red-shift of the emission peak at low temperature is generally attributed to the influence of lattice thermal expansion.[47] When the temperature decreases, the energy level of the valence band will increase with the shrinkage of the lattice constant, resulting in a smaller band gap and thus the red-shift emission. Therefore, compared with $DPCu_4Br_6$, $DPCu_4Cl_6$ has a "softer" lattice.

In addition, as the temperature decreases from 300 to 80 K, the PL intensity of $DPCu_4Cl_6$ and $DPCu_4Br_6$ increases monotonically, which is attributed to the suppression of nonradiative-decay.[48,49] The exciton activation energy (E_a) can be fit using the Arrhenius equation:[42]

$$I(T) = \frac{I_0}{1 + A\exp\left(-\frac{E_a}{k_B T}\right)} \quad (1)$$

where I_0 is the integrated PL intensity at 0 K, E_a is the exciton activation energy, and k_B is the Boltzmann constant. As shown in Fig. S11a and S11b,† E_a is 79.47 meV for $DPCu_4Cl_6$ and 124.60 meV for $DPCu_4Br_6$, which are higher than the RT thermal ionization energy (≈26 meV). High E_a indicates that photogenerated excitons in the two halides can overcome the thermal decomposition, eventually leading to the intense luminescence.[50] Meanwhile, the FWHM of $DPCu_4X_6$ (X = Cl or Br) narrows monotonously with the decrease of temperature, which is due to the weakened electron–phonon coupling during the cooling process.[49] Strong electron–phonon coupling is important for the formation of STEs, which can be evaluated by Huang-Rhys factor S. The value of S can be obtained by fitting the FWHM at different temperatures using the following formula:[51]

$$\mathrm{FWHM} = 2.36\sqrt{S}\hbar\omega_{\mathrm{phonon}}\sqrt{\cot h\frac{\hbar\omega_{\mathrm{phonon}}}{2k_B T}} \quad (2)$$

where $\hbar$ is the reduced Planck constant, ω_{phonon} is the phonon frequency and k_B is the Boltzmann constant. As shown in Fig. S11c and S11d,† the S value of $DPCu_4Cl_6$ and $DPCu_4Br_6$ is 35.8 and 22.4, respectively, which are close to those of the reported other 0D organic–inorganic hybrid metal halides with high PLQY [*e.g.*, $(C_6H_8N)_6InBr_9$:0.58% Sb (31.16),[52] $(C_{10}H_{16}N_2)SnCl_6$:3.5% Sb (28.70),[53] MA_2CuCl_3 (41.9),[54] and $(MePPh_3)_2SbCl_5$ (21.9)[30]] and higher than those of most of the conventional emission materials with low efficiency [*e.g.*, $CsPbBr_3$ (3.23),[55] CdSe (≈1)[56]]. The suitable S factors imply the existence of strong electron–phonon interactions in the $DPCu_4Cl_6$ and $DPCu_4Br_6$ SCs, which can facilitate the formation of STEs.

Although $DPCu_4I_6$ has a similar structure to $DPCu_4Cl_6$ and $DPCu_4Br_6$, the great differences in spectra indicate that their PL mechanisms are different, which prompts us to conduct more detailed photophysical characterization for $DPCu_4I_6$ SCs. As shown is Fig. 3a, the emission bands become asymmetric and red-shifted as the excitation wavelength increases from 275 nm to 425 nm. In addition, the PLE spectra also show different shapes when the detection wavelength is from 500 nm to 750 nm (Fig. 3b). The different characteristics of excitation/emission wavelength-dependent PL/PLE spectra at RT imply that the yellow luminescence of $DPCu_4I_6$ originates from multiple excited states. However, the changes of emission/excitation-dependent PLE/PL spectra are small and the lifetimes monitored at different emission wavelengths are similar, indicating that the height of the energy barriers between the excited states is low, and thus, excitons can easily cross these barriers, leading to uniform emission due to thermal equilibrium. In other words, the multiple excited states

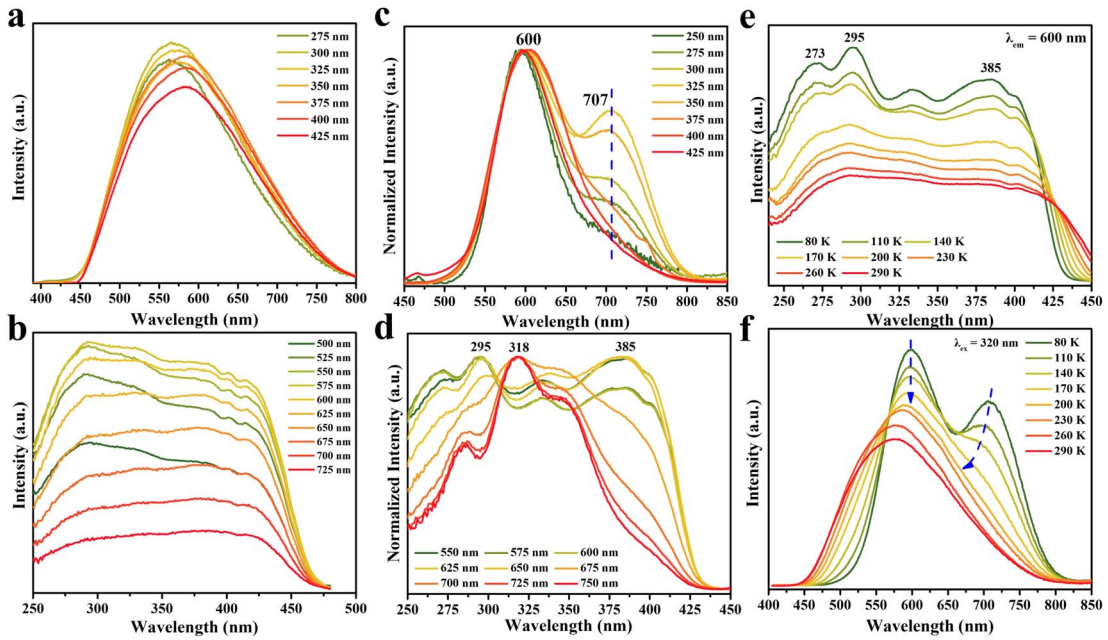

Fig. 3 Excitation and emission-wavelength dependent (a) PL and (b) PLE spectra of $DPCu_4I_6$ SCs at RT. Normalized excitation and emission-wavelength dependent (c) PL and (d) PLE spectra of $DPCu_4I_6$ SCs at 80 K. Temperature-dependent (e) PLE and (f) PL spectra of $DPCu_4I_6$ SCs.

in $DPCu_4I_6$ are easily coupled at RT to result in the bright yellow emission, and a similar behavior is also observed in $(1,3\text{-dppH}_2)_2Cu_4I_8\cdot H_2O$[57] and $Na_4(18\text{-crown-6})_5In_2Cu_4Br_{14}\cdot 8H_2O$.[58]

Moreover, the excitation wavelength-dependent PL spectra at 80 K clearly reveal the attractive dual-band emission of $DPCu_4I_6$ (Fig. 3c). Under 250 nm excitation, the PL spectrum shows a main peak on the high energy side (HE peak, ~600 nm) and a shoulder peak on the low energy side (LE peak, ~707 nm). We note that with the decrease of excitation energy (*i.e.*, increasing excitation wavelength), the relative intensity ratio of the two emission peaks (*i.e.*, LE peak intensity/HE peak intensity) gradually increases and reaches a maximum at 325 nm excitation. The ratio decreases with increasing the excitation wavelength over 325 nm and the low energy shoulder almost disappears at excitation wavelengths >375 nm. Moreover, the emission wavelength-dependent PLE spectra at 80 K further elucidate this dual-band emission property (Fig. 3d). By monitoring at 550–650 nm (HE emission band) and 675–750 nm (LE emission band), the resultant PLE spectra are distinctly different, although they exhibit similar PLE spectral ranges. Thus, these spectral features obtained at 80 K, on the one hand, illustrate that there are two emission centers in the $DPCu_4I_6$ SCs, and on the other hand, the same PLE spectral range indicates that the excited states corresponding to the HE and LE emissions are interrelated. The TRPL of $DPCu_4I_6$ was studied at 80 K, and the decay lifetimes monitored at 600 nm or 700 nm increase with the temperature cooling, which is due to the suppression of nonradiative recombination (Fig. S12†).[59] Notably, the decay lifetimes of $DPCu_4I_6$ monitored at the two wavelengths (600 nm and 700 nm) show distinct differences at 80 K, whereas the lifetimes at RT are almost identical, demonstrating that low temperature can unveil the dual emission center and implies that temperature can change the emission states of $DPCu_4I_6$.

To explore the transition of the electronic structure from low temperature to RT more intuitively and uncover the photophysical mechanism of the double emission, temperature-dependent PLE/PL spectra of $DPCu_4I_6$ were measured in the range of 80–290 K. As shown in Fig. 3e and S13,† the PLE spectrum of $DPCu_4I_6$ shows multiple peaks whether monitored at 600 or 700 nm at low temperature, however with the increase of test temperature, the PLE profiles gradually become flat, which is attributed to the coupling of excited states in $DPCu_4I_6$.[60] The temperature-dependent PL spectrum of $DPCu_4I_6$ excited at 320 nm is shown in Fig. 3f. As noted above, $DPCuI_6$ shows a distinct dual-emission band at 80 K, and as the temperature increases, the position of the HE peak remains virtually unchanged, whereas the LE peak gradually blueshifts. When the temperature is greater than 170 K, the dual-emission profile of $DPCu_4I_6$ turns into a broadband single peak, which is consistent with the change of temperature-dependent PLE spectra (*i.e.*, the shapes of the PLE spectra monitored at 600 nm and 700 nm are different at low temperatures and tend to be consistent at high temperatures) and confirms that the dual-excited state gradually transitions from nonequilibrium at low temperature to near equilibrium at RT. Remarkably, the CIE chromaticity coordinate of $DPCu_4I_6$ shifts from yellow (0.43, 0.49) to orange (0.55, 0.44) when the temperature is decreased from RT to 80 K (Fig. S14†). Furthermore, as illustrated in Fig. S15,† under 400 nm excitation, the PL spectra of $DPCu_4I_6$ consistently show only one emission peak over the whole measured temperature range (80–290 K). The single peak is Gaussian symmetric and matches well the HE peak of the dual-band emission (upon 320 nm excitation),

indicating that a low excitation energy can only promote electrons to the level corresponding to the HE band at low temperatures. At temperatures above 170 K, the characteristics of the PL spectra recorded at 400 and 320 nm excitation are identical, indicating that thermal energy can change the excited state (*i.e.*, lowering the energy barrier), and thus the electrons, although excited by a low energy, can still reach the excitation energy level corresponding to the LE band at higher temperatures (Fig. S16†).

To gain further insights into the electron transfer mechanism of $DPCu_4X_6$, the band structures of the halides were calculated based on the density functional theory (DFT). Because the crystal structures and optical properties of the chloride and bromide are similar, we selected $DPCu_4Cl_6$ as a representative for comparison with $DPCu_4I_6$. As shown in Fig. 4a and b, the calculations show that the $DPCu_4Cl_6$ and $DPCu_4I_6$ SCs have direct band characteristics, and the bandgaps are 1.41 eV for $DPCu_4Cl_6$ and 1.55 eV for $DPCu_4I_6$. The projected density of states (PDOS) of the above two halides, shown in Fig. 4c and d, indicates that the valence band maxima (VBM) of the two materials are mainly derived from Cu-3d and X-p orbitals and their conduction band minima (CBM) are entirely derived from the orbitals of the organic cation $(C_6H_{10}N_2)^{2+}$. Furthermore, the differential charge densities corresponding to the VBM and CBM states of $DPCu_4X_6$ (X = Cl, I) also confirm that electrons are located in the organic part $(C_6H_{10}N_2)^{2+}$ and holes are sited in the $[Cu_4X_6]^{2-}$ (X = Cl, I) clusters (Fig. S17†). Moreover, it can be noted from the bands that the VBM of the above two crystals are almost flat, whereas the CBM is more dispersed. This difference can be understood based on the following reasons: (1) the neighboring $[Cu_4X_6]^{2-}$ (X = Cl, I) anions are completely isolated in space, and their interactions are very weak; (2) the distances between the organic cation $(C_6H_{10}N_2)^{2+}$ are relatively short, which can enable orbital coupling, resulting in electron delocalization.[25,61] In addition, the ultra-long PL lifetime (>40 μs) of $DPCu_4Cl_6$ may be related to the carrier distribution, *i.e.*, the photo-excited electrons and holes are spatially separated, thus prolonging the exciton lifetime. However, the RT lifetime of $DPCu_4I_6$ is only ~4 μs, which is much shorter than that of $DPCu_4Cl_6$, although they have similar band structures. The difference in emission lifetime suggests that the radiative mechanism of the iodide is unlike that of $DPCu_4Cl_6$ (from STEs).

As mentioned above, the PL color of $DPCu_4I_6$ changes with temperature. In fact, a similar phenomenon of thermochromic luminescence exists in tetranuclear cuprous iodide clusters $Cu_4I_4L_4$ and their derivatives, which is usually attributed to dual-channel electron transfer, including ^{3}CC emission and X/MLCT.[38,60,62–65] The ^{3}CC emission is a combination of halide-to-metal charge transfer (^{3}XMCT) and copper-centered d → s, p transitions and is essentially independent of the ligand nature. According to the previous reports, ^{3}CC emission is usually observed as LE emission ranging from 600 to 800 nm and with lifetimes less than 20 μs.[38,60] In most cases, the Cu–Cu bonds of Cu(I)-based luminophores in the excited state have a bonding character. During the cooling process, their distances become shorter, thus stabilizing the ^{3}CC excited state and shifting the emission to the red region.[63] The HE band is usually associated with X/MLCT, which is considered to involve transfer of electrons from π* orbitals in the organic component to inorganic metal polyhedrons. A prominent feature of this band is the stable peak position over a wide range of temperatures.[38,58] Fig. 3f shows the variation of the double emission band of $DPCu_4I_6$ with temperature, and the spectral features allow us to attribute the observed emission at 707 nm to the ^{3}CC excited state and the one at 600 nm to the X/MLCT state. The shorter Cu–Cu distance of $DPCu_4I_6$ compared with that of $DPCu_4X_6$ (X = Cl or Br) suggests that ^{3}CC emission is more likely to be realized in $DPCu_4I_6$. Besides, the PL intensity of $DPCu_4I_6$ is directly proportional to the power density, indicating the negligible contribution of permanent defects to emission (Fig. S18†). Fig. S19† illustrates the normalized PL spectra at different temperatures of the three single crystals, and it can be found that there is a large thermal broadening of the emission for chloride and bromide, while the FWHM of iodide remains unchanged essentially, implying that the emission of $DPCu_4I_6$ is not triggered by the intrinsic STE transition.[42] In fact, it is possible for the three halides to form similar self-trapped states due to their similar structures, however, compared with chlorides and bromides, iodides usually have lower self-trapping energy, which may be attributed to their different lattice deformation potentials induced by different M–X bonding.[66] The lower self-trapping energy of $DPCu_4I_6$ implies that the STEs can be thermally de-trapped even at low temperatures, and thus the bright emission of $DPCu_4I_6$ is dominated by the ^{3}CC and X/MLCT synergistic excited states. Because of the large de-trapping barrier of the chloride and bromide, STEs are more readily formed in these two halides, so they exhibit similar STE emission properties including ultra-long decay lifetimes and broadband single-peaked emission.

On the basis of the results of spectral characterization and theoretical calculations, the energy level diagrams and

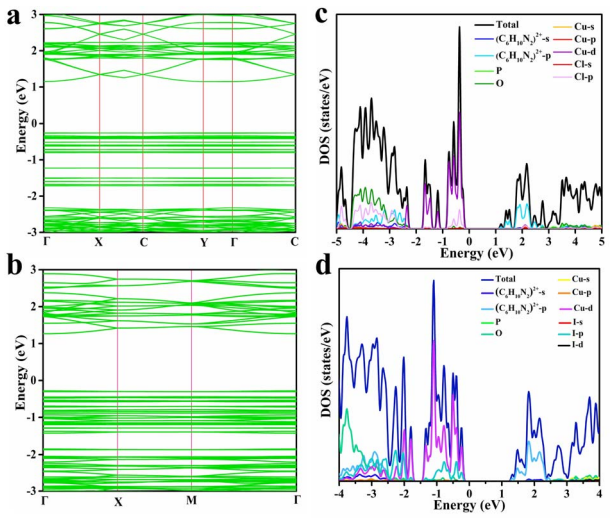

Fig. 4 Band structures of (a) $DPCu_4Cl_6$ SCs and (b) $DPCu_4I_6$ SCs. Total and orbital-projected DOSs for (c) $DPCu_4Cl_6$ SCs and (d) $DPCu_4I_6$ SCs.

electron transfer paths are proposed to describe the photophysical processes of $DPCu_4X_6$ SCs. As illustrated in Fig. 5a and b, upon photoexcitation, the electrons of $[Cu_4X_6]^{2-}$ (X = Cl or Br) units transition from the ground state to the excited state and then become free excitons (FEs). The FEs are subsequently captured by the self-trapped states resulting from lattice distortion caused by strong electron–phonon coupling. Then, the electrons located at self-trapped states return to the ground state and recombine with the holes, thereby emitting bright orange/yellow light. Owing to the "softer" lattice of $DPCu_4Cl_6$, it is prone to thermal expansion, which leads to the downward shift of its valence band and thus the blue-shifted emission with the increase of temperature. Because of the Cu–Cu distance of the two halides close to the sum of the van der Waals radii of copper(I) (2.8 Å) and the ultra-wide PLE profiles, the ^{3}CC and X/MLCT states probably exist in $DPCu_4Cl_6$ and $DPCu_4Br_6$. However, due to the formation of the self-trapping states (below the conduction band), excited electrons are easily trapped, and therefore, the ^{3}CC and X/MLCT states have negligible contribution to the luminescence of $DPCu_4Cl_6$ and $DPCu_4Br_6$. For $DPCu_4I_6$, the lower self-trapping energy makes STEs difficult to form, and the shorter Cu–Cu distance makes ^{3}CC and X/MLCT states more significant, so a synergistic effect by the ^{3}CC and X/MLCT states is proposed to understand the dual-band emission of the iodide (Fig. 5c). When the iodide is excited by high-energy UV light with wavelengths less than 320 nm, electrons in $[Cu_4I_6]^{2-}$ are pumped to the X/MLCT state, producing an HE emission band, and then a few electrons can relax into the relatively low excited state (^{3}CC state), resulting in the LE emission band. When the excitation wavelength is larger than 320 nm, the excited electrons must undergo an internal conversion process to reach the ^{3}CC state from the X/MLCT state, which decreases the population of the ^{3}CC state and weakens the LE emission, such that even LE emission disappears upon 400 nm excitation. In addition, temperature can change the excited states of $DPCu_4I_6$, and at high temperatures the two excited states of the iodide will couple leading to a lowering of the energy barrier, finally resulting in near-unify broadband yellow-light emission. In addition, long times are needed for the chloride and bromide to undergo the processes of self-trapping and de-trapping, while the iodide has almost no such processes, so it is understandable that the emission lifetime of $DPCu_4I_6$ is much shorter than that of $DPCu_4X_6$ (X = Cl or Br).

Normally, stability is an important index for SSL applications but is generally poor for cuprous-based metal halides. We first conducted thermal stability tests on the three as-synthetic crystals. The results show that the decomposition temperatures of all three halides are above 175 °C, indicating their good thermal stability (Fig. S20a†). When exposing the three crystals to air with 75% humidity, $DPCu_4Cl_6$ SCs can easily decompose and deteriorate, while $DPCu_4Br_6$ and $DPCu_4I_6$ SCs maintain their structural stability and more than 80% emission

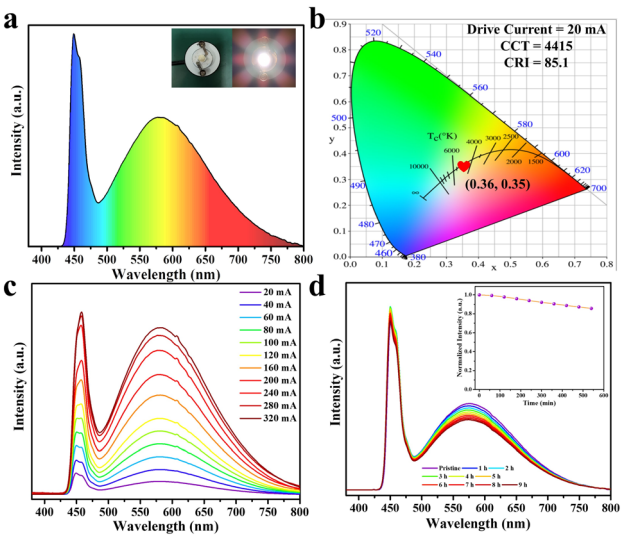

Fig. 6 (a) Luminescence spectrum of the WLED device fabricated with $DPCu_4I_6$ powder excited with a 450 nm blue light chip. The insets show photographs of a WLED with power off (left) and power on (right). (b) CIE coordinate of the WLED. (c) Drive current-dependent electroluminescence spectra. (d) Emission stability of the WLED at 20 mA driving current for 9 h. The inset shows the integrated luminous intensity of the WLED device working over different periods.

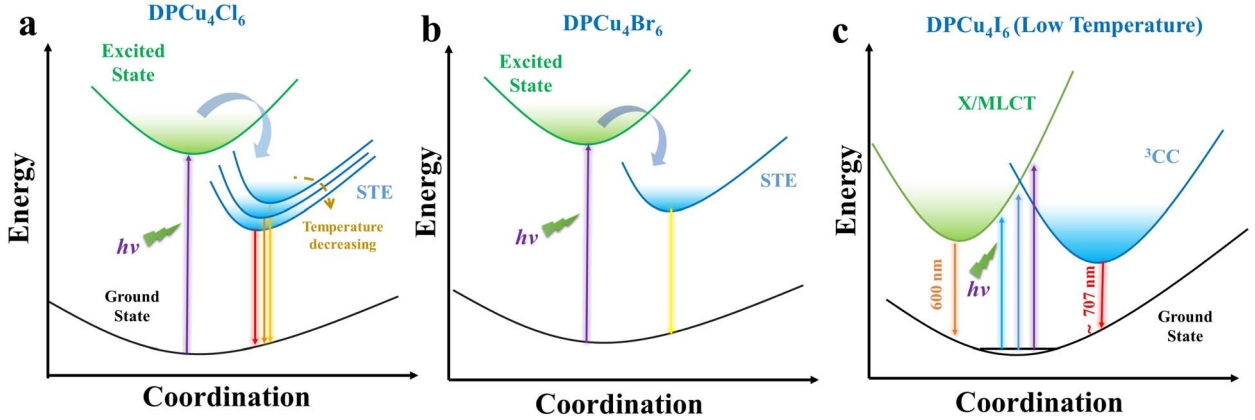

Fig. 5 Schematic of the photophysical processes in (a) $DPCu_4Cl_6$, (b) $DPCu_4Br_6$, and (c) $DPCu_4I_6$ SCs.

efficiency within two months (Fig. S20b and S20c†), suggesting that they have excellent air stability.

Benefiting from the high efficiency broadband yellow emission under the blue-light excitation, and the excellent thermal/environmental stability of $DPCu_4I_6$ SCs, a high-performance single-component WLED device was fabricated using a commercial blue light chip (445 nm) as the excitation source, as shown in Fig. 6a. Notably, high-performance warm-white-light without adding additional commercial phosphors was achieved, with a CIE color coordinate of (0.36, 0.35), a correlated color temperature (CCT) of 4415 K, a luminous efficiency of 18.41 lm W^{-1} and a color rendering index (CRI) of 85.1 (Fig. 6b), outperforming many single-component free-lead halide-based WLEDs (Table S4†). In addition, the fabricated WLED has a similar electroluminescence spectral profile at different driving currents (20–320 mA), indicating its good electroluminescence stability (Fig. 6c). More importantly, after the WLED operates at 20 mA for 9 h, the emission intensity of the device can be maintained at 85%, revealing excellent operational stability (Fig. 6d). Hence, the above results illustrate that the as-synthesized halide $DPCu_4I_6$ is a potential candidate for a single-component white light emitter.

Conclusions

In summary, three new cuprous metal halides, $DPCu_4X_6$ (X = Cl, Br, I), were successfully synthesized by a simple solution method. In the $DPCu_4Cl_6$ and $DPCu_4Br_6$ SCs, the unique crystal structures and strong electron–phonon coupling promote the formation of self-trapped excited states, leading to near-unity bright yellow/orange emission. Owing to the structural changes caused by halogen substitution (shorter Cu–Cu distance and lower self-trapping energy), the $DPCu_4I_6$ SCs exhibit dual-band emission at low temperatures, which is attributed to the synergistic effects of the ^{3}CC and X/MLCT excited states. Moreover, a WLED with a high CRI of 85.1 was fabricated by combining the $DPCu_4I_6$ powders and a blue light chip (445 nm), displaying the great potential of the obtained new materials for application in SSL. This work provides new insights into the rational design of emissive metal halides with broad excitation/emission bands, which is crucial to the development of high-performance lighting applications.

Data availability

All data are available in the manuscript and in the ESI.†

Author contributions

S. G. Zhou designed and carried out the experiments. S. G. Zhou, Y. H. Chen, X. W. Liu, and K. L. Li collected and analyzed characterization data. S. G. Zhou and T. Zhang wrote the manuscript. L. Zhou and R. X. He supervised the work and gave guidance. All authors participated in a discussion of the data. All authors have given approval to the final version of the manuscript.

Conflicts of interest

The authors declare no competing financial interest.

Acknowledgements

The authors acknowledge the financial support from the National Natural Science Foundation of China (22109130), the Fundamental Research Funds for the Central Universities (SWU-KT22031), the Natural Science Foundation of Chongqing (cstc2020jcyj-msxmX0332 and cstc2021jcyj-msxm2853), the Innovation Research 2035 Pilot Plan of Southwest University (SWU-XDZD22011) and the Program for Innovation Team Building at Institutions of Higher Education in Chongqing (CXTDX201601011).

Notes and references

1 T. T. Xuan and R. J. Xie, *Chem. Eng. J.*, 2020, **393**, 124757.
2 M. Z. Li and Z. G. Xia, *Chem. Soc. Rev.*, 2021, **50**, 2626–2662.
3 L. Zhou, J. F. Liao and D. B. Kuang, *Adv. Opt. Mater.*, 2021, **9**, 2100544.
4 T. Bai, X. Wang, Z. Wang, S. Ji, X. Meng, Q. Wang, R. Zhang, P. Han, K. L. Han, J. Chen, F. Liu and B. Yang, *Angew. Chem., Int. Ed.*, 2023, **62**, e202213240.
5 C. Zhu, J. B. Jin, M. Y. Gao, M. C. Folgueras, Y. Zhang, C. K. Lin, P. D. Yang and A. M. Oddo, *J. Am. Chem. Soc.*, 2022, **144**, 12450–12458.
6 B. B. Su, G. M. Song, M. S. Molokeev, N. N. Golovnev, M. K. Lesnikov, Z. S. Lin and Z. G. Xia, *J. Phys. Chem. Lett.*, 2021, **12**, 1918–1925.
7 Y. Han, S. J. Yue and B. B. Cui, *Adv. Sci.*, 2021, **8**, 2004805.
8 V. Morad, Y. Shynkarenko, S. Yakunin, A. Brumberg, R. D. Schaller and M. V. Kovalenko, *J. Am. Chem. Soc.*, 2019, **141**, 9764–9768.
9 L. Mao, P. Guo, M. Kepenekian, I. Hadar, C. Katan, J. Even, R. D. Schaller, C. C. Stoumpos and M. G. Kanatzidis, *J. Am. Chem. Soc.*, 2018, **140**, 13078–13088.
10 B. Luo, Y. Guo, Y. Xiao, X. Lian, T. Tan, D. Liang, X. Li and X. Huang, *J. Phys. Chem. Lett.*, 2019, **10**, 5271–5276.
11 S. Y. Zhao, W. S. Cai, H. X. Wang, Z. G. Zang and J. Z. Chen, *Small Methods*, 2021, **5**, 2001308.
12 Q. Wang, M. Q. Lyu, M. Zhang, J. H. Yun and L. Z. Wang, *J. Mater. Chem. A*, 2017, **5**, 902–909.
13 Z. J. Shi, J. Guo, Y. H. Chen, Q. Li, Y. F. Pan, H. J. Zhang, Y. D. Xia and W. Huang, *Adv. Mater.*, 2017, **29**, 1605005.
14 E. R. Dohner, E. T. Hoke and H. I. Karunadasa, *J. Am. Chem. Soc.*, 2014, **136**, 1718–1721.
15 Z. Luo, Y. Liu, Y. Liu, C. Li, Y. Li, Q. Li, Y. Wei, L. Zhang, B. Xu, X. Chang and Z. Quan, *Adv. Mater.*, 2022, **34**, 2200607.
16 X. Huang, X. T. Li, Y. Tao, S. H. Guo, J. Z. Gu, H. L. Hong, Y. G. Yao, Y. Guan, Y. A. Gao, C. Li, X. J. Lu and Y. P. Fu, *J. Am. Chem. Soc.*, 2022, **144**, 12247–12260.
17 C. Q. Jing, Q. L. Liu, C. H. Zhao, Y. Y. Zhao, C. Y. Yue and X. W. Lei, *J. Mater. Chem. C*, 2021, **9**, 15047–15055.

18 C. K. Zhou, H. R. Lin, M. Worku, J. Neu, Y. Zhou, Y. Tian, S. Lee, P. Djurovich, T. Siegrist and B. Ma, *J. Am. Chem. Soc.*, 2018, **140**, 13181–13184.
19 Y. L. Jiang and H. H. Fei, *Adv. Opt. Mater.*, 2022, **10**, 2102148.
20 Z. W. Xiao, Z. N. Song and Y. F. Yan, *Adv. Mater.*, 2019, **31**, 1803792.
21 Y. Y. Li, Z. C. Zhou, N. Tewari, M. Ng, P. Geng, D. Z. Chen, P. K. Ko, M. Qammar, L. Guo and J. E. Halpert, *Mater. Chem. Front.*, 2021, **5**, 4796–4820.
22 H. B. Li, Y. Lv, Z. N. Zhou, H. Tong, W. Liu and G. F. Ouyang, *Angew. Chem., Int. Ed.*, 2022, **61**, e202115225.
23 S. Li, J. Xu, Z. G. Li, Z. C. Zeng, W. Li, M. H. Cui, C. C. Qin and Y. P. Du, *Chem. Mater.*, 2020, **32**, 6525–6531.
24 H. Peng, X. X. Wang, Y. Tian, B. S. Zou, F. Yang, T. Huang, C. Y. Peng, S. F. Yao, Z. M. Yu, Q. R. Yao, G. H. Rao and J. P. Wang, *ACS Appl. Mater. Interfaces*, 2021, **13**, 13443–13451.
25 X. Y. Liu, F. Yuan, C. R. Zhu, J. R. Li, X. Q. Lv, G. C. Xing, Q. Wei, G. Wang, J. F. Dai, H. Dong, J. Xu, B. Jiao and Z. X. Wu, *Nano Energy*, 2022, **91**, 106664.
26 H. Peng, S. F. Yao, Y. C. Guo, R. N. Zhi, X. X. Wang, F. J. Ge, Y. Tian, J. P. Wang and B. S. Zou, *J. Phys. Chem. Lett.*, 2020, **11**, 4703–4710.
27 J. H. Wei, Y. W. Yu, J. B. Luo, Z. Z. Zhang and D. B. Kuang, *Adv. Opt. Mater.*, 2022, **10**, 2200724.
28 B. B. Su, S. N. Geng, Z. W. Xiao and Z. G. Xia, *Angew. Chem., Int. Ed.*, 2022, **61**, e202208881.
29 D. Y. Li, Y. Cheng, Y. H. Hou, J. H. Song, C. J. Sun, C. Y. Yue, Z. H. Jing and X. W. Lei, *J. Mater. Chem. C*, 2022, **10**, 3746–3755.
30 J. L. Li, Y. F. Sang, L. J. Xu, H. Y. Lu, J. Y. Wang and Z. N. Chen, *Angew. Chem., Int. Ed.*, 2022, **61**, e202113450.
31 D. Y. Li, Y. M. Sun, Z. Y. Xu, P. C. Xiao, J. H. Song, X. W. Lei, G. Chen and C. Y. Yue, *Chem. Commun.*, 2022, **58**, 9084–9087.
32 J. W. Lin, K. J. Liu, H. Ruan, N. Sun, X. Chen, J. Zhao, Z. N. Guo, Q. L. Liu and W. X. Yuan, *J. Phys. Chem. Lett.*, 2022, **13**, 198–207.
33 L. Zhou, L. Zhang, H. Li, W. Shen, M. Li and R. X. He, *Adv. Funct. Mater.*, 2021, **31**, 2108561.
34 L. Zhou, M. X. Ren, R. X. He and M. Li, *Inorg. Chem.*, 2022, **61**, 5283–5291.
35 S. Zhou, L. Zhou, Y. Chen, W. Shen, M. Li and R. He, *J. Phys. Chem. Lett.*, 2022, **13**, 8717–8724.
36 B. M. Benin, D. N. Dirin, V. Morad, M. Worle, S. Yakunin, G. Raino, O. Nazarenko, M. Fischer, I. Infante and M. V. Kovalenko, *Angew. Chem., Int. Ed.*, 2018, **57**, 11329–11333.
37 Y. C. Peng, S. H. Zhou, J. C. Jin, Q. Gu, T. H. Zhuang, L. K. Gong, Z. P. Wang, K. Z. Du and X. Y. Huang, *Dalton Trans.*, 2022, **51**, 4919–4926.
38 E. Cariati, E. Lucenti, C. Botta, U. Giovanella, D. Marinotto and S. Righetto, *Coord. Chem. Rev.*, 2016, **306**, 566–614.
39 H. Peng, Y. H. Xiao, Y. Tian, X. X. Wang, T. Huang, T. T. Dong, Y. T. Zhao, J. P. Wang and B. S. Zou, *J. Mater. Chem. C*, 2021, **9**, 16014–16021.
40 X. Y. Liu, Y. Y. Li, T. Y. Liang, W. J. Liu and J. Y. Fan, *J. Phys. Chem. Lett.*, 2022, **13**, 1373–1381.
41 M. S. Chen, C. Y. Ye, C. Q. Dai, R. J. Qi, H. M. Fu, C. H. Luo, H. Peng and H. C. Lin, *Adv. Opt. Mater.*, 2022, **10**, 2200278.
42 L. Zhou, J. F. Liao, Z. G. Huang, J. H. Wei, X. D. Wang, H. Y. Chen and D. B. Kuang, *Angew. Chem., Int. Ed.*, 2019, **58**, 15435–15440.
43 B. Chen, Y. Guo, Y. Wang, Z. Liu, Q. Wei, S. X. Wang, A. L. Rogach, G. C. Xing, P. Shi and F. Wang, *J. Am. Chem. Soc.*, 2021, **143**, 17599–17606.
44 J. C. Jin, Y. H. Peng, Y. T. Xu, K. Han, A. R. Zhang, X. B. Yang and Z. G. Xia, *Chem. Mater.*, 2022, **34**, 5717–5725.
45 Z. Y. Li, C. Y. Zhang, B. Li, C. Lin, Y. Li, L. Wang and R. J. Xie, *Chem. Eng. J.*, 2021, **420**, 129740.
46 L. Y. Lian, M. Y. Zheng, P. Zhang, Z. Zheng, K. Du, W. Lei, J. B. Gao, G. D. Niu, D. L. Zhang, T. Y. Zhai, S. Y. Jin, J. Tang, X. W. Zhang and J. B. Zhang, *Chem. Mater.*, 2020, **32**, 3462–3468.
47 R. S. Zeng, L. L. Zhang, Y. Xue, B. Ke, Z. Zhao, D. Huang, Q. L. Wei, W. C. Zhou and B. S. Zou, *J. Phys. Chem. Lett.*, 2020, **11**, 2053–2061.
48 B. B. Su, M. Z. Li, E. H. Song and Z. G. Xia, *Adv. Funct. Mater.*, 2021, **31**, 2105316.
49 D. Y. Li, J. H. Song, Y. Cheng, X. M. Wu, Y. Y. Wang, C. J. Sun, C. Y. Yue and X. W. Lei, *Angew. Chem., Int. Ed.*, 2022, **61**, e202206437.
50 J. H. Wei, J. F. Liao, L. Zhou, J. B. Luo, X. D. Wang and D. B. Kuang, *Sci. Adv.*, 2021, **7**, eabg3989.
51 Y. Y. Jing, Y. Liu, X. X. Jiang, M. S. Molokeev, Z. S. Lin and Z. G. Xia, *Chem. Mater.*, 2020, **32**, 5327–5334.
52 Q. D. Ran, Y. Zhang, J. Yang, R. X. He, L. Zhou and S. S. Hu, *J. Mater. Chem. C*, 2022, **10**, 1999–2007.
53 G. Zhang, P. Dang, H. Xiao, H. Lian, S. Liang, L. Yang, Z. Cheng, G. Li and J. Lin, *Adv. Opt. Mater.*, 2021, **9**, 2101637.
54 X. Meng, S. Ji, Q. Wang, X. Wang, T. Bai, R. Zhang, B. Yang, Y. Li, Z. Shao, J. Jiang, K. Han and F. Liu, *Adv. Sci.*, 2022, **9**, 2203596.
55 X. Z. Lao, Z. Yang, Z. C. Su, Z. L. Wang, H. G. Ye, M. Q. Wang, X. Yao and S. J. Xu, *Nanoscale*, 2018, **10**, 9949–9956.
56 V. Turck, S. Rodt, O. Stier, R. Heitz, R. Engelhardt, U. W. Pohl, D. Bimberg and R. Steingruber, *Phys. Rev. B*, 2000, **61**, 9944–9947.
57 B. B. Su, J. Jin, Y. H. Peng, M. S. Molokeev, X. B. Yang and Z. G. Xia, *Adv. Opt. Mater.*, 2022, **10**, 2102619.
58 X. Liu, Y. Li, L. Zhou, M. Li, Y. Zhou and R. He, *Adv. Opt. Mater.*, 2022, **10**, 2200944.
59 L. Zhou, J. F. Liao, Y. C. Qin, X. D. Wang, J. H. Wei, M. Li, D. B. Kuang and R. X. He, *Adv. Funct. Mater.*, 2021, **31**, 2102654.
60 J. L. Huang, B. B. Su, E. H. Song, M. S. Molokeev and Z. G. Xia, *Chem. Mater.*, 2021, **33**, 4382–4389.
61 L. Y. Lian, X. Wang, P. Zhang, J. S. Zhu, X. W. Zhang, J. B. Gao, S. Wang, G. J. Liang, D. L. Zhang, L. Gao, H. S. Song, R. Chen, X. Z. Lan, W. X. Liang, G. D. Niu, J. Tang and J. B. Zhang, *J. Phys. Chem. Lett.*, 2021, **12**, 6919–6926.
62 S. Perruchas, C. Tard, X. F. Le Goff, A. Fargues, A. Garcia, S. Kahlal, J. Y. Saillard, T. Gacoin and J. P. Boilot, *Inorg. Chem.*, 2011, **50**, 10682–10692.

63 Q. Benito, X. F. Le Goff, G. Nocton, A. Fargues, A. Garcia, A. Berhault, S. Kahlal, J. Y. Saillard, C. Martineau, J. Trebosc, T. Gacoin, J. P. Boilot and S. Perruchas, *Inorg. Chem.*, 2015, **54**, 4483–4494.

64 Y. Thefioux, M. Cordier, F. Massuyeau, C. Latouche, C. Martineau-Corcos and S. Perruchas, *Inorg. Chem.*, 2020, **59**, 5768–5780.

65 B. Li, H. T. Fan, S. Q. Zang, H. Y. Li and L. Y. Wang, *Coord. Chem. Rev.*, 2018, **377**, 307–329.

66 R. Gautier, M. Paris and F. Massuyeau, *J. Am. Chem. Soc.*, 2019, **141**, 12619–12623.